ELSEVIER

Journal of Nuclear Materials 300 (2002) 198–216

journal of nuclear materials

www.elsevier.com/locate/jnucmat

Emulation of neutron irradiation effects with protons: validation of principle

G.S. Was [a,*], J.T. Busby [a], T. Allen [b], E.A. Kenik [c], A. Jenssen [d], S.M. Bruemmer [e], J. Gan [e], A.D. Edwards [e], P.M. Scott [f], P.L. Andresen [g]

[a] *Department of Nuclear Engineering and Radiological Sciences, College of Engineering, University of Michigan, 1921 Cooley Building, 2355 Bonisteel Boulevard, Ann Arbor, MI 48109-2104, USA*
[b] *Argonne National Laboratory–West, P.O. Box 2528, Idaho Falls, ID 83403, USA*
[c] *Oak Ridge National Laboratory, Oak Ridge, TN 37831, USA*
[d] *Studsvik Nuclear AM, SE-611 82 Nyköping, Sweden*
[e] *Pacific Northwest National Laboratory, 1 Battelle Boulevard, P.O. Box 999, Richland, WA 99352, USA*
[f] *Framatome, Tour Framatome, 92084 Paris La Défense cedex, France*
[g] *General Electric Corporate Research and Development, One Research Circle, Bldg. K-1 3A39, Schenectady, NY 12309, USA*

Received 9 July 2001; accepted 29 October 2001

Abstract

This paper presents the results of the irradiation, characterization and irradiation assisted stress corrosion cracking (IASCC) behavior of proton- and neutron-irradiated samples of 304SS and 316SS from the same heats. The objective of the study was to determine whether proton irradiation does indeed emulate the full range of effects of in-reactor neutron irradiation: radiation-induced segregation (RIS), irradiated microstructure, radiation hardening and IASCC susceptibility. The work focused on commercial heats of 304 stainless steel (heat B) and 316 stainless steel (heat P). Irradiation with protons was conducted at 360 °C to doses between 0.3 and 5.0 dpa to approximate those by neutron irradiation at 275 °C over the same dose range. Characterization consisted of grain boundary microchemistry, dislocation loop microstructure, hardness as well as stress corrosion cracking (SCC) susceptibility of both un-irradiated and irradiated samples in oxygenated and de-oxygenated water environments at 288 °C. Overall, microchemistry, microstructure, hardening and SCC behavior of proton- and neutron-irradiated samples were in excellent agreement. RIS analysis showed that in both heats and for both irradiating particles, the pre-existing grain boundary Cr enrichment transformed into a ‘W’ shaped profile at 1.0 dpa and then into a ‘V’ shaped profile between 3.0 and 5.0 dpa. Grain boundary segregation of Cr, Ni, Si, and Mo all followed the same trends and agreed well in magnitude. The microstructure of both proton- and neutron-irradiated samples was dominated by small, faulted dislocation loops. Loop size distributions were nearly identical in both heats over a range of doses. Saturated loop size following neutron irradiation was about 30% larger than that following proton irradiation. Loop density increased with dose through 5.0 dpa for both particle irradiations and was a factor of 3 greater in neutron-irradiated samples vs. proton-irradiated samples. Grain boundary denuded zones were only observed in neutron-irradiated samples. No cavities were observed for either irradiating particle. For both irradiating particles, hardening increased with dose for both heats, showing a more rapid increase and approach to saturation for heat B. In normal oxygenated water chemistry (NWC) at 288 °C, stress corrosion cracking in the 304 alloy was first observed at about 1.0 dpa and increased with dose. The 316 alloy was remarkably resistant to IASCC for both particle types. In hydrogen treated, de-oxygenated water (HWC), proton-irradiated samples of the 304 alloy exhibited IG cracking at 1.0 dpa compared to about 3.0 dpa for neutron-irradiated samples,

---

[*] Corresponding author. Tel.: +1-734 763 4675; fax: +1-734 763 4540.
E-mail address: gsw@umich.edu (G.S. Was).

PII: S0022-3115(01)00751-6

although differences in specimen geometry, test condition and test duration can account for this difference. Cracking in heat P in HWC occurred at about 5.0 dpa for both irradiating particles. Thus, in all aspects of radiation effects, including grain boundary microchemistry, dislocation loop microstructure, radiation hardening and SCC behavior, proton-irradiation results were in good agreement with neutron-irradiation results, providing validation of the premise that the totality of neutron-irradiation effects can be emulated by proton irradiation of appropriate energy.

1. Introduction

Irradiation assisted stress corrosion cracking (IASCC) is a complex phenomenon involving many variables broadly subdivided among materials, environment, stress, and irradiation effects [1,2]. Of all the variables, that which demands the most resources is irradiation. Irradiation programs are extremely costly, lengthy and logistically complicated. The slow attrition in the number of test reactors, the loss of irradiated materials handling capability and the increased difficulty of irradiated materials shipment in the US and Europe has exacerbated the cost, extended the duration and compounded the complexity of such studies. The contraction of US federal and industrial support for radiation effects studies has further worsened the prospect for continued progress in the field. These developments have severely curtailed the ability of the radiation effects community to conduct meaningful and comprehensive experimental programs.

Much of the development of charged particle irradiation for the study of neutron-irradiation effects was driven by the fast breeder and fusion reactor programs. Ions of the same mass as the target material could be produced with MeV accelerators at high current, resulting in short irradiation times, little or no residual activity and low cost [3,4]. Interest in electrons as a radiation damage tool also developed [5]. Combined, these irradiation damage tools have provided considerable advancement of our understanding of the fundamental effects of irradiation on materials. Much of our understanding of the mechanisms of swelling [6,7], creep [6,8] and segregation [9–11] is due to ion irradiation experiments. The rapid damage rates and lack of residual activity are major factors favoring ion irradiation as a preferred irradiation damage tool.

Ion irradiation may well have utility beyond fundamental mechanistic studies. If it can be demonstrated that ion irradiation can emulate neutron-irradiation effects, then ion irradiation can be used to solve some of the outstanding, irradiation-induced degradation problems in current and planned reactor systems. This is a severe requirement, as any irradiation technique would need to capture the 'totality' of effects of neutron irradiation. That is, the technique must capture *all* of the effects of neutron irradiation in a practical manner. An example is IASCC that is believed to be affected by radiation-induced segregation (RIS) and the irradiated microstructure. If ion irradiation is to contribute to our understanding of IASCC, mimicking RIS alone is not adequate, even if the magnitudes and dose trends for all of the elements are faithfully reproduced from neutron irradiation. Similarly, producing the same loop size distribution is not sufficient. In light water reactors (LWRs), the dislocation loop microstructure and RIS are the dominant processes and they evolve at specific relative rates. If ion irradiation is to be used to emulate neutrons, it must match neutron irradiation in magnitude and dose evolution for both processes. If additional microstructure features are relevant (voids, second phases), then the evolution of these features must be accurately captured as well. But accurate simulation of RIS and microstructure development is still inadequate as they do not capture the full range of irradiation effects. Another potential cause of IASCC is irradiation hardening. Thus, RIS, microstructure and hardening must all occur together at the same relative rates and to the same approximate magnitudes as in neutron irradiation. Finally, to address IASCC, we need to assess IASCC susceptibility. The susceptibility of ion irradiated samples must, along with RIS, microstructure and hardening, display the same dose dependence and level of severity as that following neutron irradiation. In short, for ion irradiation to be a truly useful tool for studying IASCC, all of the effects of irradiation that may impact the behavior of the material need to be emulated in proper proportion and with the same dose evolution.

With such an onerous requirement for ion irradiation, it has become apparent that if ions are to have any chance for success in emulating all the radiation effects found in reactor systems, the best prospect lies with light ions such as hydrogen or helium. With light ions, modest energies (several MeV) result in sizable ranges in structural materials (tens of microns vs. ~1 μm for heavy ions), with the great majority of the range at a nearly constant damage rate (vs. a steep damage profile within the 1 μm range for heavy ions). A penetration depth greater than the mean grain size and the flat damage profile are the attributes of light ion irradiation that allows for the determination of irradiation-induced hardening, which, along with microstructure characterization, provides the opportunity to understand their interrelationship. The same attributes provide the opportunity to assess environmental effects in the irradiated microstructure that extend beyond the surface region (e.g. stress corrosion cracking, SCC). Typical light ion beam currents available from most MeV accelerators still provide for short term irradiation, but at rates that are one to two orders of magnitude less than those for heavy ions, thus somewhat abating the magnitude of the dose rate difference between neutrons and ions. Yet for a given damage level, radiation effects from light ions are still accelerated over that expected from neutrons, and benefit still further from the greater efficiency for producing freely migrating defects. Nevertheless, one of the prime advantages of ion irradiation, minimal activation, is still preserved. In short, light ion irradiation appears to embody the best attributes of charged particles required to simulate the various effects of neutron irradiation in materials.

There are differences in the damage process between neutron- and proton-irradiation, most notably in the nature of the displacement cascade and in the rate of damage accumulation. In principle, the irradiation conditions can be controlled to arrive at a nearly identical microstructure and microchemistry. The increased displacement rate in proton irradiation over LWR conditions (by a factor of 10^2–10^3) is balanced by a higher irradiation temperature to achieve similar diffusion kinetics and, hence, similar amounts of radiation-induced materials changes. Our current understanding of radiation effects indicates that proton irradiation closely follows neutron irradiation with regard to many characteristics [12]. Results on the dose evolution of grain boundary composition and microstructure in proton-irradiated materials provides a basis for optimism for its use in screening alternative alloys with varying compositions, and for evaluation of water chemistry and irradiation variables. For example, studies using proton irradiation have been critical in establishing the following understanding of radiation effects in austenitic alloys [12]:

- The difference in migration energies between alloy constituents is a principal, controlling factor in RIS.
- Diffusivities of alloy constituents depend on the alloy composition (bulk and local) and must be accounted for to accurately predict RIS.
- The behavior of Fe at the grain boundary is a function of the alloy composition (bulk and local), which dictates whether it enriches or depletes.
- Ordering is a significant factor influencing RIS in Ni-base austenitic alloys.
- RIS of the major elements in Fe–Cr–Ni alloys can be accounted for by vacancy diffusion without consideration for interstitial binding (not necessarily true for interstitial elements).
- Alloys with faster vacancy diffusion have a slower void nucleation rate, a longer transient swelling period, and less swelling.
- RIS and dislocation microstructure development are governed by the same point defect kinetics and tend to develop at comparable rates in a given alloy.

What is lacking is a direct comparison of proton-irradiation effects on microstructure, microchemistry and material properties on a *single alloy heat* that has also been irradiated with neutrons and characterized in the same manner.

This paper addresses that shortcoming. Specifically, the effects of proton irradiation and neutron irradiation are compared using the same heats of two austenitic stainless steel alloys: commercial purity 304SS and 316SS. Proton irradiations were carried out to doses between 0.3 and 5.0 dpa at 360 °C. Irradiated samples were characterized in terms of grain boundary composition and composition profiles, microstructure, hardness and SCC susceptibility in both normal water chemistry (NWC) and hydrogen water chemistry (HWC). Results are compared to those from the *same heats* that were irradiated up to 5.0 dpa in the Barsebäck boiling water reactor (BWR) 1 in Sweden and characterized in a similar fashion at PNNL, by Berkeley Technology Center [13], and by ABB Atom [14]. The study presented in this paper represents the first time that the effects of proton irradiation have been compared to those from neutron irradiation on the *exact same heats* of material. The prospect for utilizing proton irradiation to emulate neutron irradiation effects in austenitic alloys is evaluated on the basis of these results.

2. Experiment

2.1. Materials

The prime factor driving the selection of materials for the proof-of-principle experiments was the existence of sufficient archival material of a relevant alloy for which neutron data (microstructure, microchemistry, hardening and IASCC susceptibility) either was in existence or was in the process of being generated. The Cooperative IASCC Research (CIR) Program provided a database of all known and available neutron-irradiated materials worldwide. A detailed review of the database revealed the existence of one 304 heat (heat B) and one 316 heat (heat P) owned by ABB that met the stated criterion. Although limited microchemical/microstructural analysis of the irradiated alloys had been conducted by ABB, a program was in place at PNNL to provide full characterization of the microstructure, microchemistry and hardening at several neutron doses. The compositions of the alloys and the proton/neutron doses for which data were available are given in Table 1.

Two types of samples were used in the proton-irradiation program: transmission electron microscopy

Table 1
Bulk compositions of ABB alloys (wt%) and neutron and proton dose levels

Heat	Cr	Ni	P	Mo	Mn	Si	S	C	B	N	Doses (dpa)	
											Neutrons	Protons
304-B	18.3	8.5	0.03	0.37	1.38	0.65	0.03	0.035	<0.0004	0.068	1.0, 1.7, 3.0, 5.0	0.3, 1.0, 3.0, 5.0
316-P	16.7	12.2	0.02	2.58	1.75	0.59	0.01	0.04	0.013	0.058	1.0, 1.1, 3.0, 5.0	1.0, 3.0, 5.0

(TEM) bars and SCC specimens. Drawings of sample designs are provided in Fig. 1. All samples were made by electric discharge machining and were characterized and tested in the as-received condition. Prior to irradiation, samples were prepared using standard metallographic techniques and electropolished to a mirror finish.

Neutron irradiation was conducted on round bar tensile samples with a gage length of 25 mm, and a U-notch at the center of the gage section as shown in Fig. 1(b). All TEM analyses, hardness measurements and constant extension rate tensile (CERT) tests were conducted on these samples.

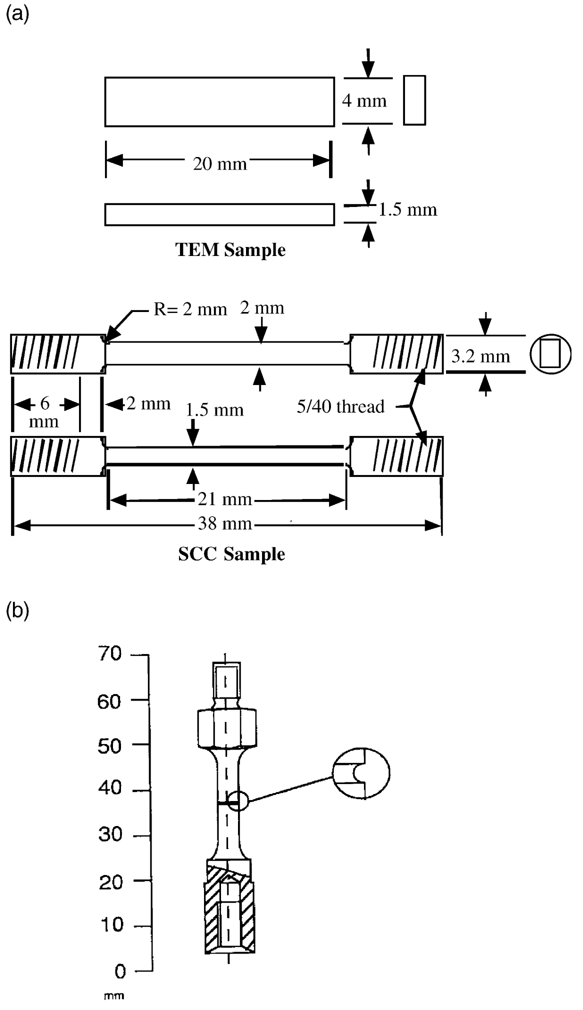

Fig. 1. Schematics of samples for (a) TEM analysis and SCC tests for proton irradiation, and (b) SCC tests using neutron irradiation.

2.2. Proton/neutron irradiation

Proton irradiations were performed using a specially designed irradiation stage attached to the main target chamber of the General Ionex Tandetron accelerator at the Michigan Ion Beam Laboratory at the University of Michigan. Irradiations were conducted using 3.2 MeV protons at a dose rate of $\approx 7 \times 10^{-6}$ dpa/s (the experimental doses and dose rates are calculated using TRIM97 [15]), resulting in a nearly uniform damage rate through the first 35 μm of the proton range (40 μm). Irradiation dose in this region ranged from 0.3 to 5.0 dpa, where dpa is calculated using TRIM97 using a displacement energy of 25 eV. Details of the irradiation procedure can be found in Ref. [16].

Nine irradiations were conducted for heats B and P at 360 ± 10 °C, spanning the dose range 0.3–5.0 dpa. After irradiation, the samples were allowed to 'cool' for 3–7 days to permit the short-lived isotopes to decay. The majority of the residual radioactivity was from β-emitters and was measured using a gas proportional detector. The activity of each sample was normalized to the sample area and inter-compared to determine the dose uniformity. Measurements were also compared against a database of measurements and a corresponding empirical model to verify the total dose. A comparison of sample activity and model predictions for all irradiation batches revealed that the greatest departure from the average activity was 5%.

Neutron irradiations were conducted in the Barsebäck 1 BWR in Sweden using vacant power range detector positions in the core. The specimens were in contact with the coolant during irradiation, and were irradiated for one, two or five reactor cycles [14]. Irradiation temperature ranged from 270 to 284 °C, depending on the axial position in the core. Fast neutron fluence ranged from 3×10^{20} n/cm^2 (0.4 dpa) to 9×10^{21} n/cm^2 (13 dpa) ($E > 1$ MeV) and fluxes from 1.5×10^{17} n/m^2 s (2×10^{-8} dpa/s) to 7.6×10^{17} n/m^2 s (10×10^{-8} dpa/s) ($E > 1$ MeV). The total error (systematic and statistical) was estimated at between −5% and +12% (worst case) and −5% and +7% (best case). The doses used in this program are given in Table 1 in units of displacements per atom (dpa) using a conversion factor of 1 dpa $= 7 \times 10^{24}$ n/m^2 s ($E > 1$ MeV) [17], that is based on a displacement energy of 40 eV, as recommended in ASTM E 521-89 [18]. The value of displacement energy is different from that (25 eV) used for the proton irradiation. For light ions at high energy, a displacement energy of 25 eV yields a displacement rate that is 1.8 times that at 40 eV.

2.3. Microchemistry characterization

Grain boundary composition and composition profiles were measured via STEM/EDS using the Philips CM200/FEG TEM–STEM at Oak Ridge National Laboratory, which is equipped with energy dispersive X-ray spectroscopy (EDS). The CM200/FEG operates with an accelerating voltage of 200 kV and an incident beam size <0.95 nm full-width at half maximum (FWHM). Spectral acquisition and analysis was done using EMiSPEC ESVision microscope control and data analysis software. Composition profiles were taken at each grain boundary with measurements taken at 1.5 nm increments. Matrix compositions were taken in each grain (corresponding to the boundaries analyzed) at distances greater than 50 nm from the boundary. Raw intensity data were then converted to weight percents using k-factors calculated from comparison of EDS-determined matrix intensities to the bulk alloy composition determined independently by electron microprobe analysis. As a result, the measured matrix composition is equal to the bulk composition listed in Table 1.

On each sample examined, at least two different grain boundaries were analyzed. During typical analysis of each grain boundary, five composition profiles were taken. In addition to the composition profiles, approximately five spot measurements were taken on each boundary, along with 10–12 spot measurements of the matrix composition which were used to determine k-factors. Finally, a matrix composition was taken from an area scan at low magnifications for each grain to ensure that the spot matrix measurements (and hence k-factors) did not contain artifacts due to local variations in the matrix composition. A 'hole-count' was also taken for each grain boundary to quantify the background EDS signal contributed from the microscope. For each irradiated condition for each heat, grain boundary composition analyses were made, on average, on five grain boundaries in two samples yielding approximately 40 grain boundary composition measurements and 20 composition profiles per condition.

Microchemical analysis of neutron-irradiated samples was performed on a JEOL 2010F FEG TEM via EDS with incident beam size <0.70 nm FWHM. A minimum of three grain boundaries was analyzed for each material with multiple measurements on each boundary and at distances of ±2 and ±10 nm from the boundary. Complete composition profiles across the boundary into the matrix were recorded out to a distance of ±5 nm in 0.5–1.0 nm steps, and to ±20 nm in 5 nm steps, for three of the boundaries. Matrix compositions in each grain were obtained in both spot mode and area mode at a distance of ~50 nm from the boundary. Profiles were taken from regions <80 nm in thickness. Background radiation was subtracted from each spectrum to yield the correct composition. The induced radioactivity resulting from neutron irradiation included Mn K peaks from the decay of Fe^{55}, so for many samples it was not possible to measure the Mn concentration reliably.

2.4. Microstructure characterization

TEM analysis of the proton-irradiated conditions of both heats B and P was conducted using a JEOL 2000FX equipped with a scanning transmission electron microscopy (STEM) unit and a charge coupled device camera. Analysis was done on the same samples used for microchemistry characterization.

The dislocation loop microstructure was examined using a two-beam condition at $g = [2\,0\,0]$ (close to $\langle 1\,1\,0\rangle$ zone axis) for bright field imaging [19] in order to show all the faulted loops ($b = a_0/3\langle 1\,1\,1\rangle$) and 2/3 of perfect loops ($b = a_0/2\langle 1\,1\,0\rangle$). The fraction of the faulted loops out of the total loops visible was determined using the weak beam dark field condition. Using diffraction conditions of $g \rightarrow 3g$ or even greater, the fringes due to stacking faults in the faulted loop can be used to identify the faulted loops. Most of the TEM pictures were taken at a magnification of 100–200k. By counting the number of loops with and without fringes, the fraction of faulted loops can be estimated.

When the loop density was high and the size was small, imaging loops in bright field mode was difficult. Therefore, most of the loop imaging was done using the fine structure diffraction effects associated with the stacking faults within the loops [20–22]. Images of Frank loops near the $\langle 0\,1\,1\rangle$ zone axis consist of two edge-on variants. The edge-on variant produces a streak in the diffraction pattern and is called a 'rel-rod'. By tilting 8–10° from the $\langle 0\,1\,1\rangle$ zone axis to form a $g = [1\,1\,3]$ 2-beam condition, the rel-rods from the Frank loops are strongly excited. Since the image from a single rel-rod shows Frank loops from only one of the four planes, the number of loops measured was multiplied by four to obtain the loop density. Rel-rod imaging provided higher resolution to show small faulted loops down to sizes ~2–3 nm in diameter. The thickness of the analyzed area was determined using contamination spots. In most cases, the TEM images were taken from areas with a thickness of 70–140 nm. A minimum of four regions (about 600 loops) on a sample were analyzed for loop density for each reported measurement.

Dislocation loops imaged using the rel-rod technique were scanned and converted to TIF-format image files from which the number and size of dislocation loops were determined. The number of loops of each size class (>2 nm) was recorded and a loop size distribution was determined, from which the average loop size and the loop density were calculated. The existence of voids was checked by changing focus of the image at a condition where no strong diffraction was excited.

Neutron-irradiated samples were imaged using either a JEOL 2010F or a JEOL 2000 TEM. Loops were imaged using the rel-rod technique described earlier. For some conditions, bright field and dark field images were also taken of the same areas for comparison. For these images, the foil was oriented near an $\langle 0\,1\,1\rangle$ zone axis with a 2-beam condition setup using the [2 0 0] reflection. Thickness was measured using convergent beam electron diffraction, which is accurate to within 5%. Foil thickness varied from 40 to 80 nm. For density measurements the micrographs were enlarged to yield a total magnification of 600–900k for loop counting.

To ensure a valid comparison between proton- and neutron-irradiated microstructures of the same heat, a benchmarking exercise was conducted in which a proton-irradiated microstructure (heat P irradiated to 3.0 dpa with protons) was analyzed using TEMs at each laboratory. The results showed that there was a discrepancy in loop density by a factor of 2.0 that was caused by different measurement techniques used on the different microscopes; see Refs. [23,24] for details. As such, all loop density measurements taken on proton-irradiated samples measured in the JEOL 2000 FX were normalized by multiplying by a factor of 2.0.

The rel-rod technique is capable of imaging defects down to 2 nm or smaller and captures much of what has historically been reported in the literature as black dots. Though some amount of defects below the imaging resolution of the instruments persists, it is instrument dependent and is less significant with higher resolution microscopes. Further, sample preparation of proton-irradiated samples sometimes involved ion milling which can introduce sub nanometre defects in the foil as artifacts of the sample preparation process. Therefore, characterization of the defect structure below the imaging resolution of the microscopes was not pursued.

2.5. Hardness measurements

Hardening in proton-irradiated samples was measured by Vickers indentation (Micromet II) with a load of 25 g. This low load was necessary in order to confine the plastic zone ahead of the indenter tip to the range of the protons (~40 μm) to ensure that un-irradiated material was not being sampled. Samples for hardness testing were mechanically wet-polished using SiC paper (grit 300–4000) and then electropolished for 3 min in a 60% phosphoric acid –40% sulfuric acid solution. A total of 50 hardness indents were made for each irradiation condition. An average and standard deviation were determined for each condition. The hardness value of the un-irradiated condition was subtracted from that of the irradiated condition to arrive at a hardness increase due to irradiation.

Hardening of neutron-irradiated samples was measured by Vickers indentation and shear punch testing. Vickers hardness was conducted using the same procedure as was used for proton-irradiated samples but with a 200 g load. Shear punching was conducted by driving a 1 mm diameter punch at a constant rate of 0.002 mm/s through a TEM-sized disk (nominally 0.25 mm thick and 3 mm in diameter) and constrained on both the upper and lower surfaces. The load on the punch is measured as a function of specimen displacement, from which yield and maximum loads can be determined. Previous work by Hamilton et al. [25] has shown that shear yield and maximum strengths obtained by shear punch test methods can be correlated to tensile yield and ultimate tensile strength, respectively.

2.6. Stress corrosion cracking experiments

Constant extension rate tests on proton-irradiated samples were conducted in a multiple-specimen CERT test system capable of straining four samples in parallel, providing identical conditions within a given test. A schematic of this system is shown in Fig. 2. The CERT setup consisted of an autoclave capable of sustaining pressures up to 3000 psi and temperatures up to 360 °C, a load frame, and a computer driven, 30 kN load train for straining of the samples. The titanium autoclave with a capacity of 1.8 l was sealed using deformable stainless steel O-rings.

CERT tests were performed in either BWR NWC or HWC. NWC and HWC conditions are given in Table 2. Conditions for NWC were selected to achieve maximum discrimination of SCC susceptibility [2]. Dilute sulfuric acid was added to maintain the conductivity at 0.2 μS/cm. The dissolved oxygen composition was selected to arrive at a value of the corrosion potential of about +150 mV_{SHE} [26]. This potential agreed with the value used in the ABB-atom experiments [9]. The potential and conductivity were in the regime where the sensitivity to material condition is greatest. The HWC condition was chosen to produce a corrosion potential of ~ -500 mV_{SHE}, which was close to the value used in the ABB experiments [14]. The electrochemical potential was verified for both the NWC and HWC environments using a Cu/CuO reference electrode with a yttria stabilized zirconia membrane, in conjunction with an EG&G Model 173 potentiostat.

Experimental parameters were tracked continuously during the CERT test using a PC-based monitoring

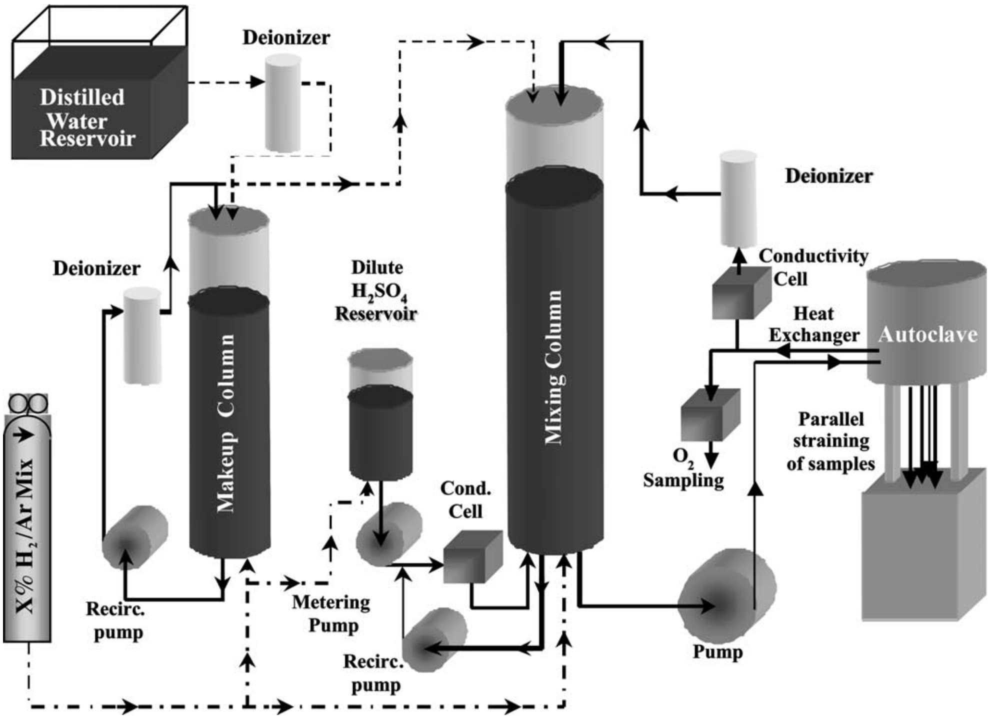

Fig. 2. Schematic of SCC test loop for proton-irradiated samples, using CERT for multiple specimens.

Table 2
CERT test conditions

Parameter	NWC		HWC	
	Protons	Neutrons	Protons	Neutrons
Sample design	Tensile	U-notched tensile	Tensile	U-notched tensile
Temperature (°C)	288	275	288	275
Extension rate (s^{-1})	3×10^{-7}	1×10^{-8}	3×10^{-7}	1×10^{-8}
Test duration	To failure	168 h	To failure	168 h
pH (28 °C)	6.0	NA	6.2	NA
Conductivity (μS/cm)	0.2	0.2	0.1	0.1
O_2 concentration (ppb)	2000	300–400	<5	<1
H_2 concentration (ppb)	–	–	560	70
Corrosion potential (mV_{SHE})	+140	+100 to +200	−500	−500

NA = not available.

system. Water temperature, system pressure, water conductivity, load for each sample, and extension were all monitored and recorded every 1000 s. Typical outlet conductivity was 0.2 μS/cm.

Fractography was performed on each sample following the CERT test. Any oxide layer developed during the CERT test was removed using a 10% nitric acid solution. Samples were ultrasonically cleaned in the acid solution for 20 min and then cleaned in acetone for 5 min. This procedure was repeated until all oxide was removed. Specimens were examined in a Philips XL30/FEG SEM. Intergranular fracture was characterized by measuring the area of IG facets compared to the area of the fracture surface. Since the proton irradiation only affected the first 40 μm of the irradiated face and IG cracking was only observed in the first 40 μm, the fracture surface was defined by the 40 μm proton penetration depth. This semi-quantitative method was used to compare the relative amount of cracking between proton and neutron irradiation.

SCC tests of neutron-irradiated samples were performed in a loop attached to the feed side of the reactor water cleanup system in Barsebäck 1 [14]. The test loop was located close to the reactor to achieve a short transportation time for water from the reactor pressure vessel to the autoclaves. The actual transport time from the reactor pressure vessel downcomer to the CERT autoclave was 50 s. The water chemistry for both NWC and HWC conditions is shown in Table 2.

CERT tests were conduced on round bar specimens fabricated with a gage length of 25 mm and a mid-gage machined U-notch (Fig. 1(b)) [14]. Prior to initiation of testing, each ABB CERT specimen was preloaded to 80–90% of its yield stress in the un-irradiated condition at 275 °C. The specimens were strained at a rate of approximately 1×10^{-8} s^{-1} at the notch root. In most cases, testing was stopped after 168 h (one week) when the average elongation over the gage length was 0.6%. Subsequent to disassembly all unruptured specimens were strained to fracture in air at room temperature. Fracture surfaces were studied in a SEM and on each specimen the maximum IGSCC crack depth was estimated. Results were reported as maximum crack penetration divided by the test time.

The notched design of the ABB CERT samples, the limited amount of deformation in the autoclave (0.6% and 168 h), and the practice of subsequently pulling the samples to failure in air makes direct comparison of %IG fracture in neutron-irradiated samples and proton-irradiated samples challenging. Nevertheless, these represent the closest comparison between proton and neutron-irradiation effects on IASCC available, and with some simplifying assumptions, valuable comparisons can be made.

3. Results and discussion

3.1. Radiation-induced segregation

The evolution of grain boundary microchemistry with dose is compared for proton and neutron irradiations in Figs. 3–8. Fig. 3 shows the development of the grain boundary chromium concentration profile as a function of dose for heats B and P for both neutron and proton irradiations. Complete composition profiles for both particle irradiations exist at only 0 and 1.0 dpa (Fig. 3(a)). In these cases, the agreement is excellent. The Cr enrichment at 0 dpa develops into a ‘W’ shaped profile at 1 dpa that is most pronounced in heat P for both particle irradiations. Fig. 3(b) shows the full progression of the grain boundary chromium composition profile as a function of dose for heats B and P. By 5.0 dpa, the Cr profile has transformed from being enriched to distinct depletion at the grain boundary with minimal evidence of the prior ‘W’ shape.

Fig. 4 is a detailed comparison of the grain boundary profiles for Cr, Ni and Si in heat P following 1.0 dpa for neutrons and protons. The ‘W’ shape Cr concentration profile at this dose provides, perhaps, the most difficult test of the capability of proton irradiation to emulate neutron irradiation in terms of radiation-induced segregation. The data show that in all aspects of comparison; including trend, spatial extent and magnitude, the composition profiles resulting from the two types of irradiation are virtually indistinguishable (any differences are within experimental uncertainty). Further, while Cr forms a distinct ‘W’ profile, both Ni and Si show rather normal grain boundary enrichment.

Figs. 5–8 show the behavior of the minimum measured compositions of Cr, and Mo and the grain boundary compositions of Ni and Si for both proton- and neutron-irradiated heats B and P as a function of dose. Proton data points represent averages of 20–25 grain boundary measurements on 2–3 grain boundaries in 1–2 samples. Both Cr and Mo display a ‘W’ shape profile and, hence, the minimum composition of the solute is not at the grain boundary but rather at the troughs of the ‘W’. All of the major trends are consistent between the two irradiations. Cr and Mo concentrations drop quickly with dose and then level out at doses above 3 dpa for both irradiations, as shown in Figs. 5 and 6, respectively. The amounts of segregation are comparable but slightly greater for neutron irradiation compared to proton irradiation. Fig. 5 includes the comparison of minimum-measured Cr concentration in proton-irradiated heats B and P to the available literature data for neutron-irradiated austenitic stainless steels [27–34]. Ni and Si (Figs. 7 and 8) show much different grain boundary segregation behavior than do Cr and Mo (Figs. 5 and 6) for both irradiations. Ni and Si increase with dose in a more linear fashion through 5.0 dpa. The proton-irradiation data for Ni and Si agree extremely well with neutron data for heat B and show a little less segregation for heat P at the highest dose. Additional data on RIS in similar alloys is given in Refs. [35,36].

Following proton irradiation, the grain boundary Mn content decreased with increased dose in heats B and P. For both alloys, the grain boundary Mn concentration dropped from the bulk level (1.38 and 1.75 wt% for heats B and P, respectively) to less than 1.0 wt% by 5.0 dpa. No corresponding measurements were taken for neutron-irradiated samples because of contributions to the Mn peak from decay of Fe^{55} created by transmutation during irradiation.

3.2. Microstructure

The primary microstructure feature in samples irradiated with protons and neutrons is small, faulted Frank loops. The size distributions of Frank loops in proton- and neutron-irradiated samples of heats B and P are compared for similar doses in Fig. 9. Both sets of data show that the size distribution for heat B is narrower

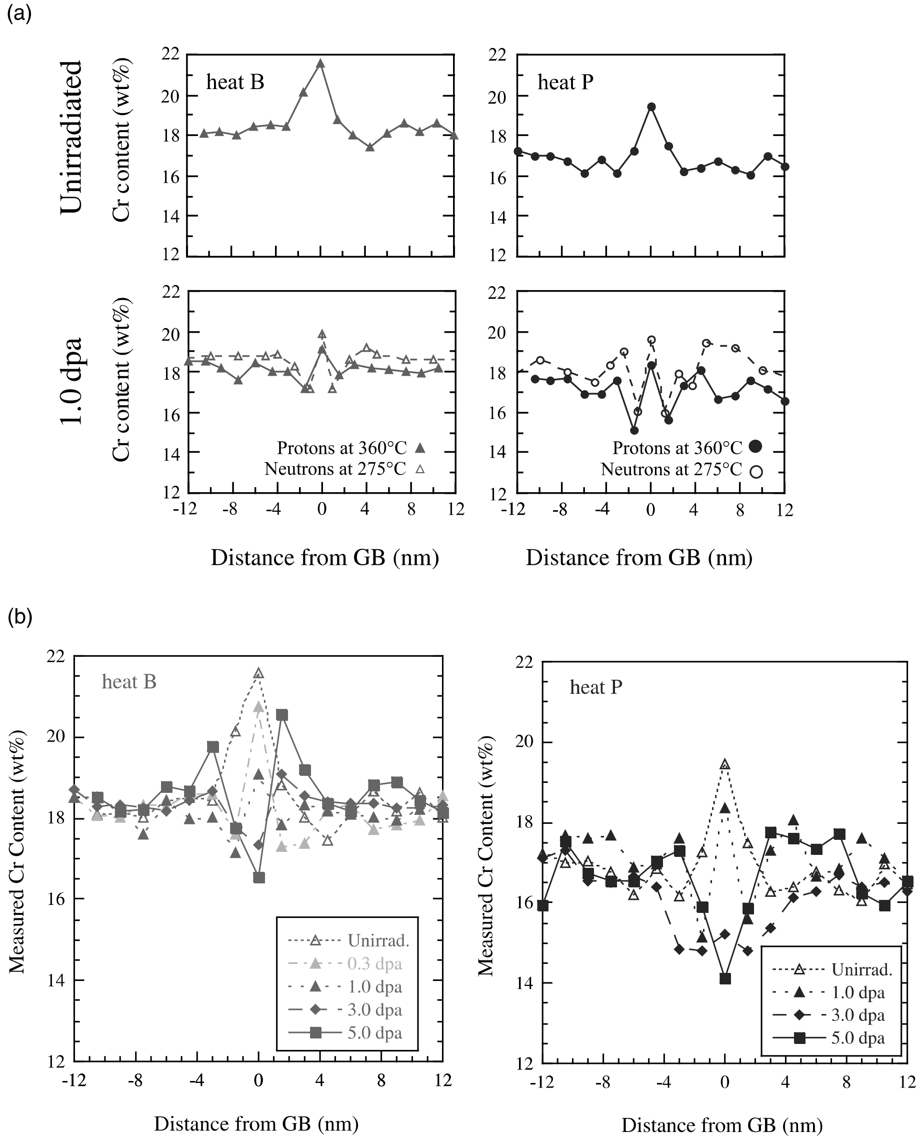

Fig. 3. Evolution of grain boundary Cr concentration profiles in heats B and P with dose for (a) un-irradiated, and proton and neutron irradiation at 1.0 dpa, and (b) for proton irradiation through 5.0 dpa.

and peaks at a smaller loop size than that for heat P. The agreement between neutron and proton results at each of the doses for which comparable data exist is very good in terms of both the shape of the distribution and the peak and average values. Even subtle features such as a flattening in the heat P distribution at 9–10 nm are consistent between the two 1 dpa irradiations. One point of difference is a broadening of the size distribution with dose of neutrons, but not of protons. Overall, the loop size distributions for proton- and neutron-irradiated samples are in excellent agreement.

The dose dependencies of loop size and faulted loop density for heats B and P irradiated with protons and with neutrons are plotted in Fig. 10. The magnitudes of the loop diameters and the dependence on dose differ somewhat. Results from proton-irradiated samples show a sharp increase in loop size that saturates around 1.0 dpa and remains at the saturation value (6–8 nm) through 5.0 dpa. Loop size for the neutron-irradiated samples rises sharply up to 1.0 dpa, then continues to increase through 3–5 dpa, but at a slower rate, resulting in loop sizes in the 8–10 nm range.

The loop density for neutron irradiation is higher than that for proton irradiation by a factor of between 1.5 and 3 (Fig. 10(b)). The neutron results show a very slow increase in the heat B loop density through 1.7 dpa,

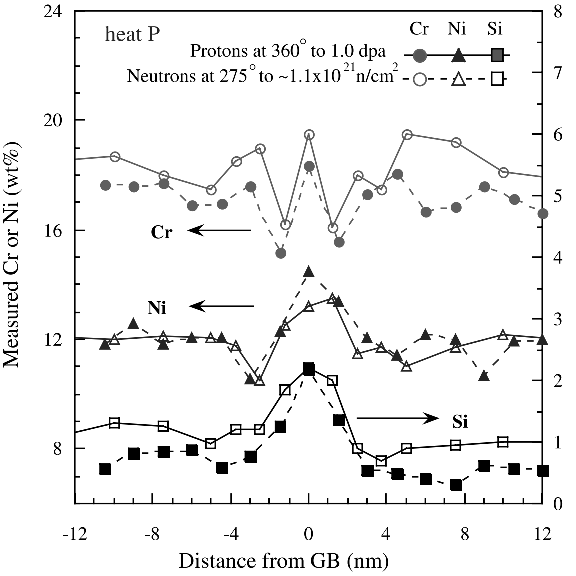

Fig. 4. Comparison of Cr, Ni, and Si segregation profiles following proton and neutron irradiation of heat P to 1.0 dpa.

followed by a more rapid increase between 1.7 and 5.0 dpa. Only the neutron-irradiated, heat B sample at 5.0 dpa gives a loop density greater than a factor of 3 above that from protons. Experimental errors are such that densities within a factor of 2 are considered to be experimentally equal using this technique. Both sets of data show that the loop density increases with dose. The

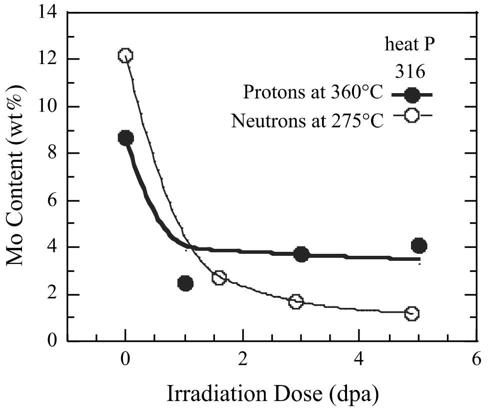

Fig. 6. Dose dependence of minimum Mo composition for heat P irradiated with protons at 360 °C and with neutrons at 275 °C.

proton-irradiated results show that the loop density saturates at about 3.0 dpa and is virtually unchanged between 3.0 and 5.0 dpa. For heat P, both sets of data show a steady increase in loop density through 5.0 dpa.

Denuded zones adjacent to grain boundaries were observed in some neutron-irradiated conditions, but not in any proton-irradiated conditions. In neutron-irradiated heat B, denuded zones were observed at the lowest (0.7 dpa) and intermediate (1.6 dpa) doses but not at the highest dose (5.0 dpa). In heat P, the low and intermediate doses were not examined, but denuded zones were observed after 2.9 and 4.9 dpa. Denuded zone width is

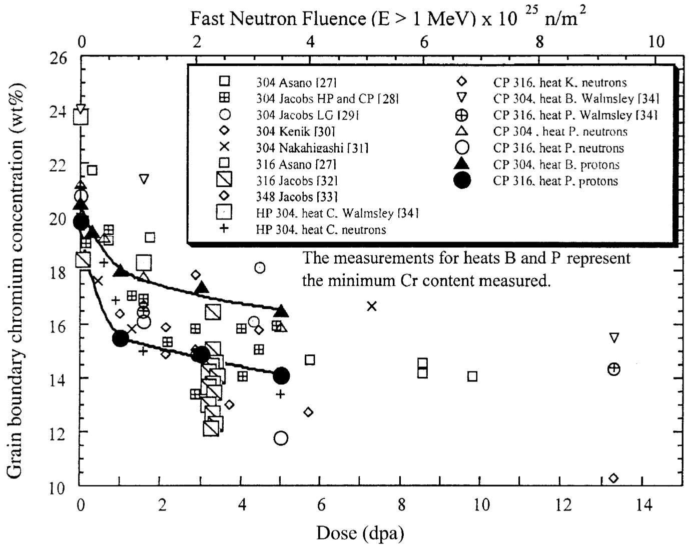

Fig. 5. Comparison of minimum measured Cr composition as a function of dose for proton-irradiated heats B and P with neutron-irradiated heats B and P and available data from the open literature for other austenitic stainless steels neutron-irradiated under LWR conditions [27–34]. Heats C and K were used in the same study of neutron-irradiation effects as heats B and P.

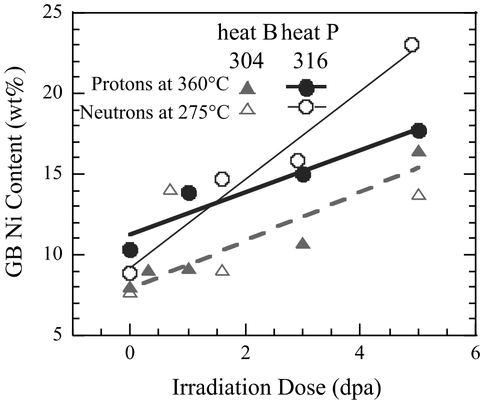

Fig. 7. Dose dependence of grain boundary Ni for heats B and P irradiated with protons at 360 °C and with neutrons at 275 °C.

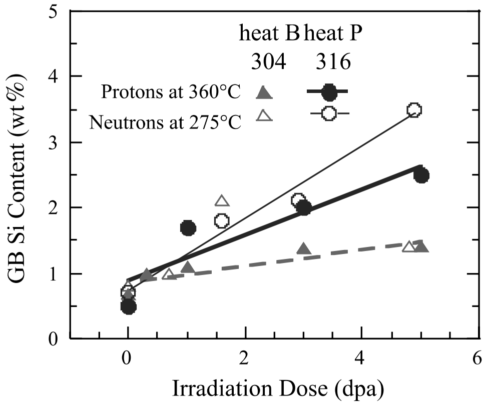

Fig. 8. Dose dependence of grain boundary Si for heats B and P irradiated with protons at 360 °C and with neutrons at 275 °C.

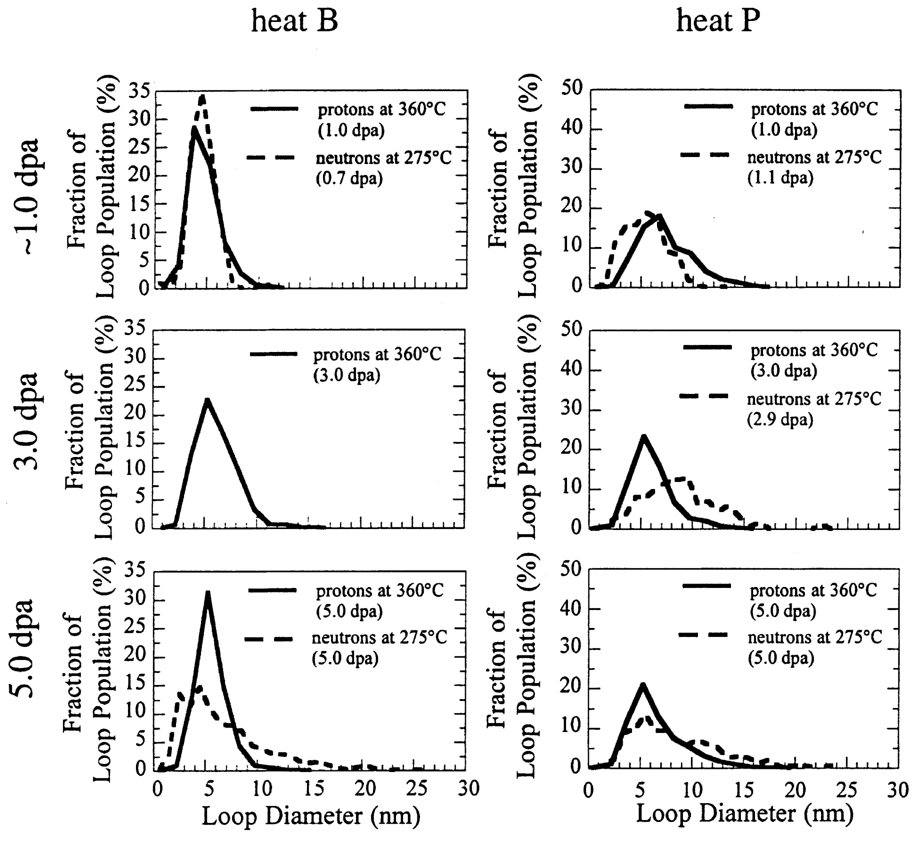

Fig. 9. Comparison of faulted loop size distributions in heats B and P irradiated to 5.0 dpa with protons at 360 °C and with neutrons at 275 °C.

greater in heat P than in heat B. The width decreases with dose for both alloys. Additional 304 and 316 alloys were examined in this study (without complementary proton irradiation) and denuded zones were clearly observed in two of the three 304 SS alloys and the same with the 316 SS alloys. However, the presence of de-

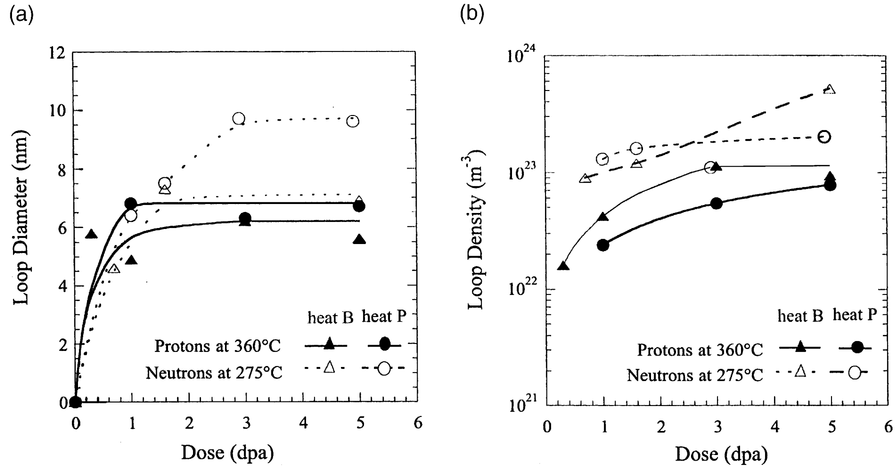

Fig. 10. Dose dependence of (a) faulted loop size and (b) faulted loop density for heats B and P irradiated with protons at 360 °C and with neutrons at 275 °C.

nuded zones was not investigated at all available doses for each alloy. Denuded zones were clearly observed at an intermediate dose (1.7 dpa) in one 304 alloy and at two different doses (1.0 and 3.7 dpa) in one of the 316 alloys. In the other 304 and 316 alloys irradiated under the same conditions, true denuded zones were not observed at 1.2 and 1.1 dpa, respectively. Rather, small clusters of loops (different in size from the nearby matrix) were observed near the boundaries in these two alloys. The factors controlling the formation and disappearance of these zones are not well understood [37]. Jenssen et al. [38] observed denuded zones in heats B and P at neutron fluence above 1×10^{21} n/cm^2. However, depleted zones are not consistently observed in neutron-irradiated materials. The reason for the appearance of the denuded zones in the neutron-irradiated conditions and the absence of denuded zones in the proton-irradiated conditions is unknown.

There was no evidence of voids in either heat at any dose by either proton or neutron irradiation. This observation is consistent with the literature [39] in that voids are typically not observed in low dose irradiation near 300 °C. The results are also complementary to earlier studies that showed void nucleation under similar proton irradiation conditions in high purity 304 alloys but not in commercial alloys [40,41]. Both results underscore the importance of impurities, specifically silicon, in commercial alloys that act to suppress void nucleation at low temperatures [42].

In neither neutron nor proton irradiation were any additional phases formed during irradiation. As reviewed by Maziasz et al. [43,44], irradiation-induced precipitation and second phases are formed in austenitic stainless steels during irradiation at higher doses and temperatures typical of fast reactor core conditions. However, at temperatures below ~300 °C and doses below ~10 dpa, radiation-induced phase formation is rarely observed.

3.3. Radiation hardening

The hardening resulting from proton- and neutron-irradiation is presented in terms of yield strength increase in Fig. 11. Yield strength was calculated from hardness measurement (protons and neutrons) [45] or from shear punch measurement (neutrons) [25] using the following relations:

$$\Delta\sigma_y = 3.55\ \Delta H_v, \tag{1}$$

where $\Delta\sigma_y$ is the increment in yield strength (MPa), and ΔH_v is the increment in hardness (kg/mm^2), and

$$\sigma_y = m(\tau_{\text{meas}} - \tau_o), \tag{2}$$

where σ_y is the tensile yield strength (MPa), τ_{meas} is the measured shear yield strength (MPa), τ_o is the offset parameter (MPa), and m is a constant. Yield strengths determined from Eq. (1) for proton and neutron irradiation and from Eq. (2) for neutron irradiation are shown in Fig. 11. Both sets of data showed that in heat B, initial rapid hardening was followed by saturation by 3 dpa, and in heat P, hardening continued to increase with dose through 5.0 dpa. Yield strength determined from hardness measurements of neutron-irradiated samples agree well with those from shear punch tests on neutron-irradiated samples and hardness on proton-irradiated samples with the exception of the 5.0 dpa sample, which showed considerably higher hardness.

Yield strength determined by both methods for both heats are compared in Fig. 12 to the existing data base

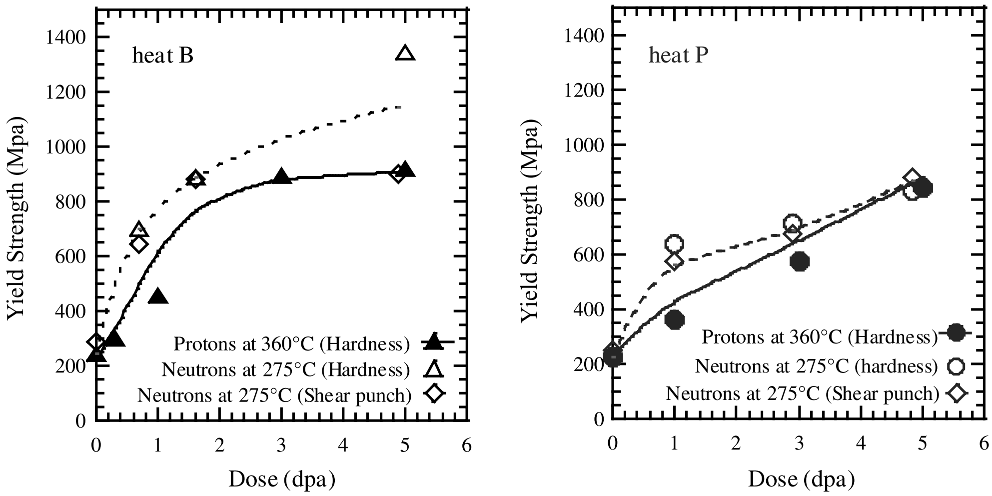

Fig. 11. Dose dependence of yield strength as determined from hardness (proton- and neutron-irradiated) and shear punch (neutron-irradiated) measurements on samples irradiated up to 5.0 dpa.

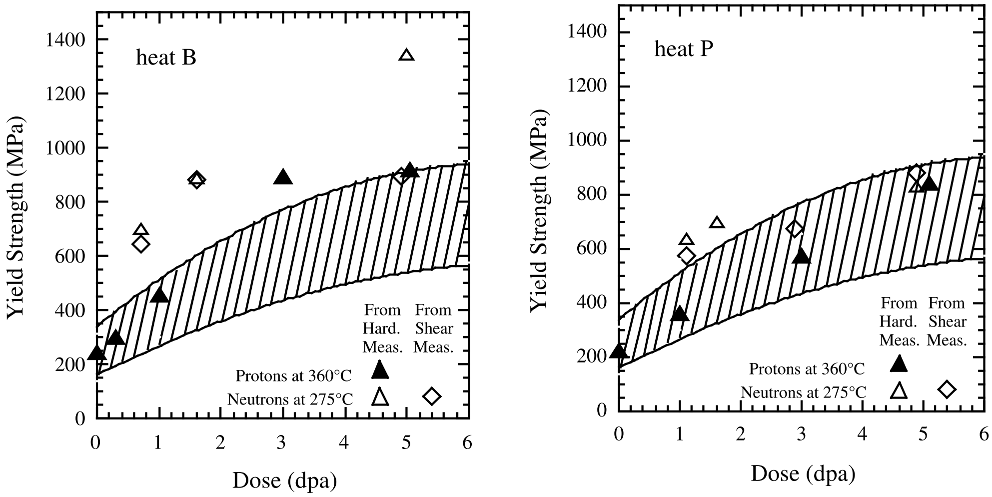

Fig. 12. Comparison of yield strength of proton- and neutron-irradiated heats B and P (from hardness and shear punch measurements) with existing data (shown by the cross-hatched bands) for neutron-irradiated 300-series stainless steels taken from Ref. [46].

on hardening of 300 series austenitic stainless steels irradiated and tested at about 300 °C [46]. The solid lines represent a 2σ bound to the literature data, which refers to samples irradiated *and* tested at ~300 °C. Results for both proton- and neutron-irradiation in this study are within the 2σ bounds or above the upper bound of the literature data. Because the neutron irradiation was conducted at 275 °C (and the proton was conducted at a temperature designed to simulate the neutron irradiation), and hardening was measured at room temperature, the strengths were expected to fall on the high side of the 300 °C database, as shown in Fig. 12.

Fig. 13 shows the agreement between yield strength as determined from hardness/shear punch measurements and that determined from microstructural characterization of proton- and neutron-irradiated samples of heats B and P using the dispersed barrier hardening model:

$$\Delta\sigma_y = \alpha M \mu b (Nd)^{1/2}, \tag{3}$$

where α is the faulted loop barrier strength (0.4), M is the Taylor factor (3.06), μ is the shear modulus (76 GPa), b is the Burgers vector (0.255 nm), N is the loop density and d is the loop size. Yield strength calculated

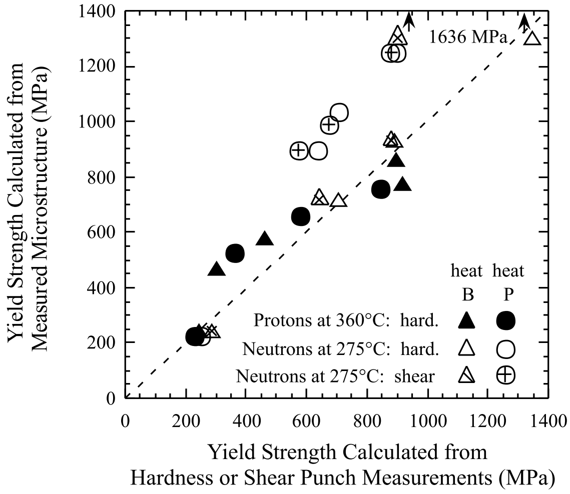

Fig. 13. Agreement between yield strength as determined from hardness and shear punch measurements and that determined from microstructure for proton- and neutron-irradiated heats B and P.

from hardness/shear punch measurement and from microstructure for both proton and neutron irradiation lie close to the 45° line for low to intermediate strength, indicating that, according to the dispersed barrier hardening model, the measured hardness was in agreement with that expected from the measured microstructure. The agreement was not as good at high strength levels where that predicted from microstructure exceeded that measured by hardness/shear punch for neutron-irradiated samples.

3.4. Stress corrosion cracking

3.4.1. Normal water chemistry

The SCC behavior of proton-irradiated heats B and P is compared to that of neutron-irradiated heats B and P in Figs. 14 and 15. Direct quantitative comparison is complicated by a number of factors. In the neutron-irradiated specimens, the %IG is based on the entire fracture surface area, even though tests were conducted for nominally 168 h and then pulled to failure in air afterward, producing a large amount of post-SCC ductile rupture. For proton-irradiated samples, the %IG fracture reported refers to the *irradiated area* of the fracture surface for samples pulled to failure in water. Since CERT tests of proton-irradiated samples were run to failure, the fracture surface of the irradiated area is often composed of IG and TG failure only, with little ductile fracture, especially at higher doses. Therefore, while both are measures of the propensity for IGSCC, the measurements are not completely equivalent.

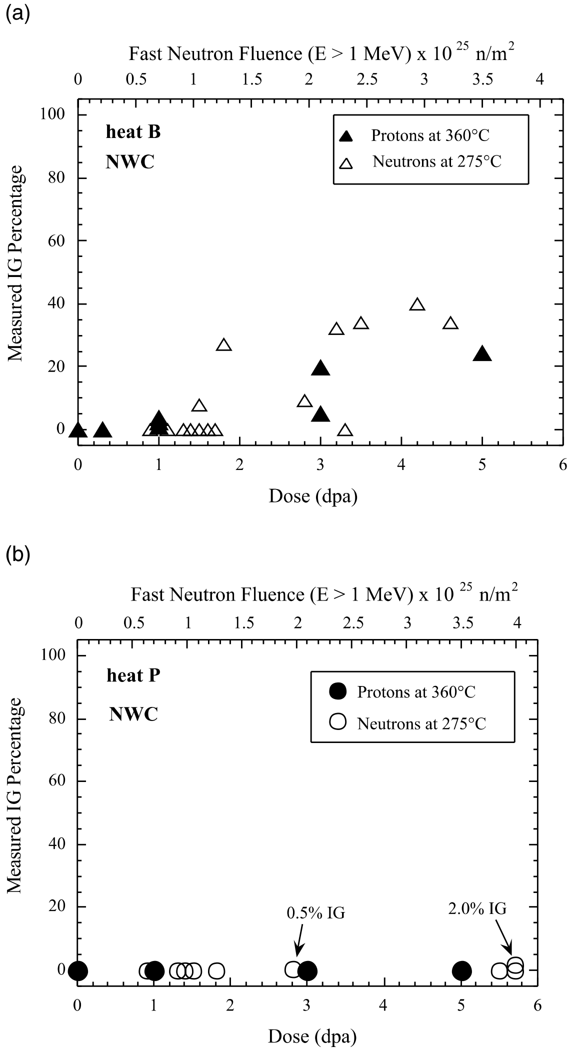

Fig. 14. IG cracking susceptibility of neutron- and proton-irradiated heat B (a), and heat P (b), strained in NWC.

Cracking of proton-irradiated heat B in NWC showed excellent agreement with neutron-irradiated samples in terms of the dose dependence and the degree of cracking (Fig. 14(a)). In both cases, IG cracking is first observed at about 1.0 dpa. This is significant in that a dose of 1.0 dpa has been considered as a 'threshold' dose for IASCC in NWC [1]. While this dose is not a true threshold in the sense that it depends on alloy and water chemistry and measurement resolution, the two data sets agree in the onset of IASCC at around 1.0 dpa. The results also show that the %IG increases with dose through 5.0 dpa. This is a commonly observed behavior for 304SS alloys stressed in NWC [9]. The onset of cracking at 1.0 dpa also agrees with the literature.

Fig. 14(b) shows the IG cracking behavior of heat P in NWC for both proton- and neutron-irradiated samples. Samples of heat P irradiated with protons up to 5.0 dpa show only ductile fracture and no evidence of IG

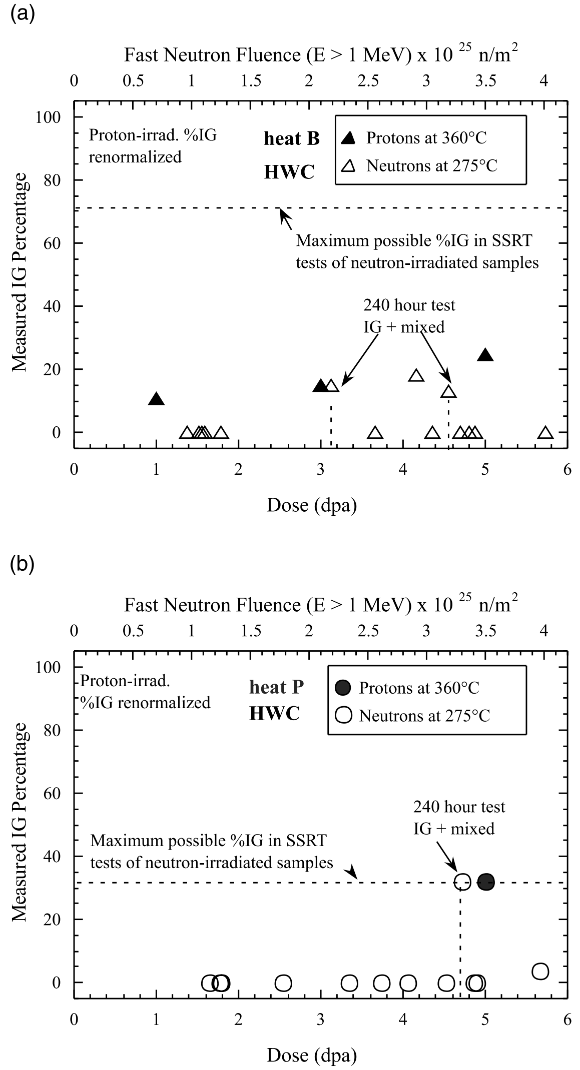

Fig. 15. IG cracking susceptibility of neutron- and proton-irradiated heat B (a), and heat P (b) strained in HWC.

cracking. Further, heat P samples irradiated with protons exhibit the same ductile fracture morphology as the unirradiated heat P, suggesting that the apparent threshold fluence for heat P in NWC is above 5.0 dpa. Below 6.0 dpa, only two neutron-irradiated heat P samples showed evidence of IGSCC. In both cases, the amount of IG cracking was less than 2%. Results of IASCC of proton-irradiated samples in NWC are in excellent agreement with those from neutron-irradiated samples.

3.4.2. Hydrogen water chemistry

The comparison of IGSCC in proton- and neutron-irradiated samples tested in HWC is shown in Fig. 15. Because crack depths are smaller in the neutron-irradiated samples and the ductile fraction is larger, the need to compare neutron results to proton results on a common scale is greater in the case of HWC. A method was developed to factor out a portion of the ductile rupture in the neutron-irradiated samples caused by post-test fracture in air. The maximum measured crack depth was used to estimate the maximum possible %IG fraction that could occur during CERT tests of the notched, round-bar samples, assuming equal radial penetration on the circumference of the specimen. This value is shown as a dashed line in Fig. 15(a) and (b). The values of %IG for the proton-irradiated samples are then normalized to these values and plotted for comparison. The effect of this renormalization is to provide a more accurate comparison of the %IG cracking between the two test procedures. The renormalization was not applied to the NWC results since the effect was small (only a 3% difference) for heat B and was not required for heat P samples since there was essentially no IGSCC in NWC.

Results show that proton-irradiated heat B samples exhibit IG cracking at 1.0 dpa and the %IG increases monotonically with dose through 5.0 dpa. Data from neutron irradiation showed that only one sample with doses below 5.0 dpa had IG cracking. However, two samples (~3 and ~4.5 dpa) tested for 240 h rather than the nominal value of 168 h both failed with a relatively large percentage of IG + mixed mode cracking. This observation moves the apparent threshold dose to a lower value and indicates that the test time (or strain) may be an important factor affecting the observed threshold dose and the %IG cracking.

Fig. 15(b) shows the results for heat P tested in HWC. The 5.0 dpa proton-irradiated sample showed about 30% IG cracking after a CERT test to failure. Of all the neutron-irradiated samples pulled for 168 h, only one showed a small amount of IG cracking at a dose of ~5.5 dpa. Two samples were subjected to 240 h of straining in the same environment. One revealed only TG cracking, but the other, irradiated to ~4.5 dpa, showed about 32% IG + mixed mode cracking on the fracture surface. These results are in good agreement with that of the 5.0 dpa proton-irradiated sample and again suggest that the amount of IG cracking and the threshold dose are functions of test time or strain.

In summary, a qualitative and a semi-quantitative comparison shows that SCC of proton-irradiated samples is consistent with the trends in the neutron-irradiated samples for both heats B and P tested in NWC and HWC.

4. Other issues

4.1. Retained hydrogen

A potential concern with proton irradiation is the retention and the subsequent effect of the implanted hydrogen atom on the microstructure and mechanical properties of the sample. As shown by Hunn et al. [47], there is very little retained hydrogen at implantation temperatures above 100 °C in low energy, high dose deuterium implantation experiments. Therefore, it is unlikely that significant hydrogen is retained in the 360 °C irradiations used in these experiments. Direct measurement of hydrogen content in the 40 μm depth is difficult and complicated by numerous factors. However, the prime concern is the effect on mechanical properties as hydrogen is known to embrittle austenitic alloys in the −50 to 150 °C temperature range. In an earlier study [48], constant extension rate experiments were conducted on HP304SS in room temperature air and in Ar at 288 °C to determine whether retained hydrogen can lead to cracking. By conducting the experiments in air, the role of the aqueous environment was removed. Tests in Ar at 288 °C were conducted as companion tests to those conducted in water at 288 °C, in which cracking occurred readily in HP304SS. Neither test resulted in cracking of irradiated samples, in sharp contrast to the result in 288 °C water in which an average of 22 cracks per sample were observed in a total of six CERT tests. These test results indicate that implanted hydrogen is not a factor in the observed IGSCC of austenitic alloys.

4.2. Dose equivalence

Another issue that arises with ion irradiation is dose equivalence. Early experiments and analysis of ion irradiation indicated that light ions may be significantly more effective in producing freely migrating defects that are responsible for the development of RIS and the dislocation microstructure [49,50]. Some proton data exist that support this argument as well [51]. However, recent experiments with both proton and electron irradiation (which should have the greatest difference in freely migrating defect fraction compared to neutrons) of model pressure vessel steel ferritic steel alloys showed no difference in the dose dependence of the change in yield strength increase as compared to neutrons. In fact, the hardening vs. dose data for proton, electron and neutron irradiation fall on the same line for each of three model alloys spanning a factor of 100 in dose range [52]. Early results on proton-irradiated HP304SS and the results in this study on commercial purity 304SS and 316SS also showed no difference between protons and neutrons in the dose dependence of property or microstructure changes.

Experiments and modeling of loop nucleation and growth provide some clues to the cause of the dose equivalence in the irradiated microstructure. Gan et al. [53] have suggested that the reduction of in-cascade interstitial clusters in proton irradiation is compensated by a higher interstitial survival rate in cascades due to the higher cascade efficiency for proton irradiation. Nevertheless, the important issue is whether protons can produce the same damage morphology as neutrons and that the doses are linearly related. A second factor influencing the dose dependence of microstructure and microchemistry evolution was the raster-scanning mode used for proton irradiation [54]. In raster-scanning, a given location was under the beam only a fraction of the time, producing an effect similar to pulsed irradiation. In these experiments, the instantaneous dose rate was about 40 times the average dose rate, resulting in a high local displacement rate, greater point defect recombination, and an effective reduction in the freely migrating defect fraction that governs microchemistry and microstructure development.

Finally, it should be noted that the use of a 25 eV displacement energy results in a dose that is about a factor of 1.8 greater than that at 40 eV. The effect would be to scale the proton dose down by a factor of 1.8 relative to the neutron dose. However, the scale factor on the dose axis is merely a measure of how fast the irradiation effects occur, and does not alter the values or dependencies.

4.3. Transmutation

One effect of neutrons that cannot be simulated is the transmutation of alloying or impurity elements in the irradiated material. Transmutation reactions that produce H, He or other light, mobile elements can affect subsequent performance of the alloy such as increasing swelling caused by He stabilization of void nuclei. Because of the relatively low energy of proton irradiation, such transmutation does not occur in stainless steels. Thus, processes that depend on the production of transmutation products, and the rate of production vis à vis the displacement rate, cannot be emulated by protons. Given the success in emulating neutron-irradiation effects and IASCC behavior in austenitic stainless steels, transmutation is probably not a significant factor.

4.4. Background radiation

An advantage of working with low activity samples is that the low radiation level presents no problem in making composition measurements using EDS. This was evident in the analysis of Mn concentration, which was impossible to determine in highly activated neutron-irradiated samples. There is no problem with proton-irradiated samples, thus allowing a more complete characterization of composition changes at the grain boundaries.

5. Conclusions

Comparison of radiation induced segregation, irradiated microstructure, radiation hardening and IASCC susceptibility of the *same* heats of proton- and neutron-irradiated CP304SS and CP316SS resulted in the following.

(1) For both irradiations, Cr and Mo deplete at the grain boundaries and Ni and Si enrich at the grain boundaries with Fe enriching or depleting depending on the relative compositions of the alloying elements. The magnitudes of enrichment and depletion of all elements are comparable for both irradiations. The spatial extent of the enrichment/depletion profile is nearly identical for both irradiations. The dose dependence is the same up through the highest dose examined of 5.0 dpa.

(2) At all doses, the microstructure consists predominantly of small (<10 nm average diameter), faulted Frank loops. Loop size distributions between particle types agree extremely well at low doses. Loop size is slightly smaller for proton irradiation and the loop density is lower by a factor of about 3. Denuded zones adjacent to grain boundaries are sometimes observed following neutron irradiation, but not following proton irradiation. There is no evidence of cavity formation up through 5.0 dpa for irradiation by either particle type.

(3) The magnitude of hardening and the dose dependence are nearly identical up through 5.0 dpa for both alloys. Hardening and saturation occur more quickly in heat B than in heat P. By 5.0 dpa, the hardness of heat P is less than that for heat B and saturation had yet to occur. Yield strength increases as determined from hardness measurements and from microstructure (using the dispersed barrier hardening model) were in excellent agreement up through 5.0 dpa for both neutron and proton irradiation.

(4) IASCC of heat B in NWC occurs at about 1.0 dpa and the amount of IG fracture increases with increasing dose through 5.0 dpa for both particle types. Heat P is much more resistant to cracking in NWC for both particle types, exhibiting no cracking in the proton-irradiated samples up through 5.0 dpa, and only two instances of cracking in neutron-irradiated samples through 6.0 dpa. In HWC, there is less of a distinction between heats as proton- and neutron-irradiated samples of both heats showed cracking at doses at or below 5.0 dpa.

Overall, the agreement in RIS, microstructure, irradiation hardening and susceptibility to IASCC between neutron- and proton-irradiated CP304SS and CP316SS is excellent. This unique study validates the utility of proton irradiation in emulating the full extent of neutron-irradiation effects in austenitic stainless steels.

Acknowledgements

The authors wish to thank Victor Rotberg and Ovidiu Toadar for their support in conducting proton irradiations. Michigan Ion Beam Laboratory for Surface Modification and Analysis and the Electron Microbeam Analysis Laboratory, University of Michigan, provided facilities for irradiation and microstructure analysis. The authors appreciate the guidance and support provided by Larry Nelson and Karen Gott throughout the project. Support for this work was provided by the Cooperative IASCC Research (CIR) program through EPRI contracts WO 4068-20 and WO 4068-26, and by the Office of Basic Energy Sciences, US Department of Energy under contract DE-AC06-76RLO 1830 for the PNNL authors.

References

[1] S.M. Bruemmer, E.P. Simonen, P.M. Scott, P.L. Andresen, G.S. Was, J.L. Nelson, J. Nucl. Mater. 274 (1999) 299.

[2] G.S. Was, P. Andresen, JOM 44 (4) (1992) 8.

[3] S. Ishino, N. Sekimura, J. Nucl. Mater. 174 (1990) 158.

[4] D.J. Mazey, J. Nucl. Mater. 174 (1990) 196.

[5] M. Kiritani, J. Nucl. Mater. 216 (1994) 220.

[6] L.K. Mansur, J. Nucl. Mater. 216 (1994) 97.

[7] L.K. Mansur, M.H. Yoo, J. Nucl. Mater. 85&86 (1979) 523.

[8] F. Garner, J. Nucl. Mater. 117 (1983) 177.

[9] R.A. Johnson, N.Q. Lam, J. Nucl. Mater. 69&70 (1978) 424.

[10] N.Q. Lam, A. Kumar, H. Wiedersich, in: H.R. Brager, J.S. Perrin (Eds.), Effects of Radiation on Materials: Eleventh Conference, ASTM STP 782, American Society for Testing and Materials, West Conshohocken, PA, 1982, p. 985.

[11] L.E. Rehn, P.R. Okamoto, in: F.V. Nolfi Jr. (Ed.), Phase Transformations During Irradiation, Applied Science, New York, 1983, p. 247.

[12] G.S. Was, T.R. Allen, J.T. Busby, J. Gan, D. Damcott, D. Carter, M. Atzmon, E.A. Kenik, J. Nucl. Mater. 270 (1999) 96.

[13] A. Jenssen, L.G. Ljungberg, J. Walmsley, S. Fisher, Corrosion 54 (1) (1998) 48.

[14] A. Jenssen, L.G. Ljungberg, in: Proceedings of the Seventh International Symposium on Environmental Degradation of Materials in Nuclear Power Systems—Water Reactors, NACE International, Houston, TX, 1995, p. 1043.

[15] J.F. Ziegler, J.P. Biersack, TRIM 97 program, IBM Corp., Yorktown, NY.

[16] D.L. Damcott, J.M. Cookson, V.H. Rotberg, G.S. Was, Nucl. Instrum. and Meth. B 99 (1995) 780.

[17] P.L. Andresen, F.P. Ford, S.M. Murphy, J.M. Perks, in: Proceedings of the Fourth International Symposium on Environmental Degradation of Materials in Nuclear Power Systems—Water Reactors, National Association of Corrosion Engineers, Houston, TX, 1990, p. 1.

[18] Standard practice for neutron radiation damage simulation by charged-particle irradiation, ASTM Designation E 521-89, Annual Book of ASTM Standards, vol. 12.02, Amer-

ican Society for Testing and Materials, Philadelphia, PA, 1989, p. D-9.
[19] C. Brown, in: J.V. Venables (Ed.), Developments in Electron Microscopy and Analysis, Academic Press, New York, 1976, p. 405.
[20] D.J. Edwards, E.P. Simonen, S.M. Bruemmer, in: Proc. Microstructural Processes in Irradiated Materials, Materials Research Society, Pittsburgh, PA, 2001, p. R2.7.
[21] D.J. Edwards, E.P. Simonen, S.M. Bruemmer, submitted to J. Nucl. Mater.
[22] D.J. Edwards, E.P. Simonen, S.M. Bruemmer, in: Proceedings of the Ninth International Symposium on Environmental Degradation of Materials in Nuclear Power Systems—Water Reactors, TMS, Warrendale, PA, 1999, p. 1007.
[23] J. Gan, PhD thesis, University of Michigan, 1999.
[24] J. Gan, G.S. Was, J. Nucl. Mater. 297 (2001) 161.
[25] M.L. Hamilton, F.A. Garner, G.L. Hankin, R.G. Faulkner, M.B. Toloczko, in: M.L. Hamilton, A.S. Kumar, S.T. Rosinski, M.L. Grossbeck (Eds.), Effects of Radiation on Materials: Nineteenth International Symposium, ASTM STP 1366, American Society for Testing and Materials, West Conshohocken, PA, 2000, p. 1003.
[26] P.L. Andresen, in: R.H. Jones (Ed.), Stress-corrosion Cracking, Materials Performance and Evaluation, ASM International, Materials Park, OH, 1992, p. 181.
[27] K. Asano, K. Fukuya, K. Nakata, M. Kodoma, in: D. Cubicciotti (Ed.), Proceedings of the Fifth International Symposium on Environmental Degradation of Materials in Nuclear Power Systems—Water Reactors, Monterey, CA, American Nuclear Society, La Grange Park, IL, 1992, p. 838.
[28] A.J. Jacobs, in: A.S. Kumar, D.S. Gelles, R.K. Nanstad, E.A. Little (Eds.), Sixteenth International Symposium on Radiation on Materials, ASTM STP 1175, American Society for Testing and Materials, Philadelphia, PA, 1993, p. 902.
[29] A.J. Jacobs, G.E.C. Bell, C.M. Shepperd, G.P. Wozadlo, in: D. Cubicciotti, E.P. Simonen, R.E. Gold (Eds.), Proceedings of the Fifth International Symposium on Environmental Degradation of Materials in Nuclear Power Systems—Water Reactors, American Nuclear Society, La Grange Park, IL, 1992, p. 917.
[30] E.A. Kenik, J. Nucl. Mater. 187 (1992) 239.
[31] S. Nakahigashi, M. Kodama, K. Fukuya, S. Nishimura, S. Yamamoto, K. Saito, T. Saito, J. Nucl. Mater. 179–181 (1991) 1061.
[32] A.J. Jacobs, G.P. Wozadlo, K. Nakata, S. Kasahara, T. Okada, S. Kawano, S. Suzuki, in: R.E. Gold, E.P. Simonen (Eds.), Proceedings of the Sixth International Symposium on Environmental Degradation of Materials in Nuclear Power Systems—Water Reactors, The Metallurgical Society, 1993, p. 597.
[33] A.J. Jacobs, R.E. Clausing, M.K. Miller, C.M. Shepperd, in: Proceedings of the Fourth International Symposium on Environmental Degradation of Materials in Nuclear Power Systems—Water Reactors, National Association of Corrosion Engineers, Houston, TX, 1990, p. 14.
[34] J. Walmsley, B.P. Spellward, S. Fisher, A. Jenssen, in: R.E. Gold, E.P. Simonen (Eds.), Proceedings of the Seventh International Symposium on Environmental Degradation of Materials in Nuclear Power Systems—Water Reactors, NACE International, Houston, TX, 1995, p. 985.
[35] S.M. Bruemmer, in: P.F. Ford, G.S. Was, L. Nelson (Eds.), Proceedings of the Tenth International Symposium on Environmental Degradation of Materials in Nuclear Power Systems—Water Reactors, NACE International, Houston, TX, in press.
[36] S.M. Bruemmer, D.J. Edwards, V.Y. Gertsman, E.P. Simonen, in: Proc. Microstructural Processes in Irradiated Materials, Materials Research Society, Pittsburgh, PA, 2001, p. R2.1.
[37] E.P. Simonen, D.J. Edwards, S.M. Bruemmer, in: Proceedings of the Ninth International Symposium on Environmental Degradation of Materials in Nuclear Power Systems—Water Reactors, TMS, Warrendale, PA, 1999, p. 1107.
[38] A. Jenssen, L.G. Ljungberg, K. Pettersson, J. Walmsley, in: Proceedings of the Eighth International Symposium on Environmental Degradation of Materials in Nuclear Power Systems—Water Reactors, American Nuclear Society, La Grange Park, IL, 1997, p. 785.
[39] S.I. Porollo, Y.V. Konobeev, A.M. Dvoriashen, V.M. Krigan, F.A. Garner, in: P.F. Ford, G.S. Was, L. Nelson (Eds.), Proceedings of the Tenth International Symposium on Environmental Degradation of Materials in Nuclear Power Systems—Water Reactors, NACE International, Houston, TX, in press.
[40] J.T. Busby, T.R. Allen, J. Gan, G.S. Was, E.A. Kenik, in: Proceedings of the Eighth International Symposium on Environmental Degradation of Materials in Nuclear Power Systems—Water Reactors, American Nuclear Society, La Grange Park, IL, 1997, p. 758.
[41] M. Sagisaka, T. Fukuda, Y. Isobe, F. Garner, G.M. Bond, B.H. Sencer, G. Was, T. Kamada, K. Matsueda, in: Proceedings of the Tenth International Conference on Environmental Degradation of Materials in Nuclear Power Systems—Water Reactors, August 2001, NACE International, Houston, TX, in press.
[42] F.A. Garner, A.S. Kumar, in: F.A. Garner, N.H. Packan, A.S. Kumar (Eds.), Radiation-induced Changes in Microstructure: Thirteenth International Symposium, ASTM STP 955, American Society for Testing and Materials, Philadelphia, PA, 1987, p. 289.
[43] S.J. Zinkle, P.J. Maziasz, R.E. Stoller, J. Nucl. Mater. 206 (1993) 266.
[44] P.J. Maziasz, J. Nucl. Mater. 205 (1993) 118.
[45] H.R. Higgy, F.H. Hammad, J. Nucl. Mater. 55 (1975) 177.
[46] G.R. Odette, E.G. Lucas, J. Nucl. Mater. 179–181 (1991) 572.
[47] J.D. Hunn, B. Lewis, E.H. Lee, in: Proceedings of the 2nd International Topical Meeting on Nuclear Applications of Accelerator Technology, American Nuclear Society, La Grange Park, 1998, p. 375.
[48] J. Cookson, R. Carter, D. Damcott, M. Atzmon, G.S. Was, J. Nucl. Mater. 202 (1993) 104.
[49] L.E. Rehn, R.C. Birtcher, J. Nucl. Mater. (1993) 31.
[50] L.E. Rehn, J. Nucl. Mater. 174 (1990) 144.
[51] T. Aoki, T. Fukuda, Y. Isobe, A. Hasegawa, M. Sato, K. Abe, K. Matsueda, Y. Nishida, in: F.P. Ford, S.M. Bruemmer, G.S. Was (Eds.), Ninth International

Symposium on Environmental Degradation of Materials in Nuclear Power Systems—Water Reactors, The Minerals, Metals and Materials Society, Warrendale, PA, 1999, p. 1099.

[52] Q. Yu, G.S. Was, L.M. Wang, R. Odette, D.E. Alexander, in: Proc. Microstructural Processes in Irradiated Materials, Materials Research Society, Pittsburgh, PA, 2001, p. B6.2.1.

[53] J. Gan, G.S. Was, R.E. Stoller, J. Nucl. Mater. 299 (2001) 53.

[54] J. Busby, PhD thesis, University of Michigan, 2001.